

EVALUATING THE DISENTANGLEMENT OF DEEP GENERATIVE MODELS WITH MANIFOLD TOPOLOGY

Sharon Zhou, Eric Zelikman, Fred Lu, Andrew Y. Ng, Gunnar Carlsson, Stefano Ermon
 Computer Science & Math Departments, Stanford University
 {sharonz, ezelikman, fredlu, ang, ermon}@cs.stanford.edu,
 carlsson@stanford.edu

ABSTRACT

Learning disentangled representations is regarded as a fundamental task for improving the generalization, robustness, and interpretability of generative models. However, measuring disentanglement has been challenging and inconsistent, often dependent on an ad-hoc external model or specific to a certain dataset. To address this, we present a method for quantifying disentanglement that only uses the generative model, by measuring the topological similarity of conditional submanifolds in the learned representation. This method showcases both unsupervised and supervised variants. To illustrate the effectiveness and applicability of our method, we empirically evaluate several state-of-the-art models across multiple datasets. We find that our method ranks models similarly to existing methods.

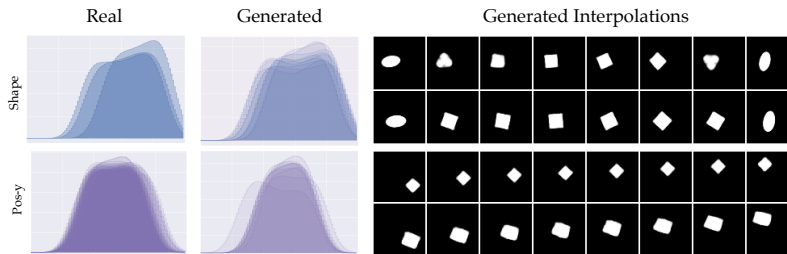


Figure 1: Factors in the *dSprites* dataset displaying topological similarity and semantic correspondence to respective latent dimensions in a disentangled generative model, as shown through Wasserstein RLT distributions of homology and latent interpolations along respective dimensions.

1 INTRODUCTION

Learning disentangled representations is important for a variety of tasks, including adversarial robustness, generalization to novel tasks, and interpretability (Stutz et al., 2019; Alemi et al., 2017; Ridgeway, 2016; Bengio et al., 2013). Recently, deep generative models have shown marked improvement in disentanglement across an increasing number of datasets and a variety of training objectives (Chen et al., 2016; Lin et al., 2020; Higgins et al., 2017; Kim and Mnih, 2018; Chen et al., 2018b; Burgess et al., 2018; Karras et al., 2019). Nevertheless, quantifying the extent of this disentanglement has remained challenging and inconsistent. As a result, evaluation has often resorted to qualitative inspection for comparisons between models.

Existing evaluation metrics are rigid: while some rely on training additional ad-hoc models that depend on the generative model, such as a classifier, regressor, or an encoder (Eastwood and Williams, 2018; Kim and Mnih, 2018; Higgins et al., 2017; Chen et al., 2018b; Glorot et al., 2011; Grathwohl and Wilson, 2016; Karaletsos et al., 2015; Duan et al., 2020), others are tuned for a particular dataset (Karras et al., 2019). These both pose problems to the metric’s reliability, its relevance to different models and tasks, and consequently, its applicable scope. Specifically, reliance on training and tuning external models presents a tendency to be sensitive to additional hyperparameters and introduces partiality for models with particular training objectives, e.g. variational methods (Chen et al., 2018b; Kim and Mnih, 2018; Higgins et al., 2017; Burgess et al., 2018) or adversarial

methods with an encoder head on the discriminator (Chen et al., 2016; Lin et al., 2020). In fact, this reliance may provide an explanation for the frequent fluctuation in model rankings when new metrics are introduced (Kim and Mnih, 2018; Lin et al., 2020; Chen et al., 2016). Meanwhile, dataset-specific preprocessing, such as automatically removing background portions from generated portrait images (Karras et al., 2019), generally limits the scope of the metric’s applicability because it depends on the preprocessing procedure and may otherwise be unreliable without it.

To address this, we introduce an unsupervised disentanglement metric that can be applied across different model architectures and datasets without training an ad-hoc model for evaluation or introducing a dataset-specific preprocessing step. We achieve this by examining topology, an intrinsic property of a manifold that typically exhibits modes corresponding to high-density regions, surrounded by low-density regions (Cayton, 2005; Narayanan and Mitter, 2010; Goodfellow et al., 2016). Our method investigates the topology of these low-density regions (holes) by estimating homology, a topological invariant that characterizes the distribution of holes on a manifold. We first condition the manifold on each latent dimension and subsequently measure the homology of these conditional submanifolds. By comparing homology, we examine the degree to which conditional submanifolds continuously deform into each other. This provides a notion of topological similarity that is higher across submanifolds conditioned on disentangled dimensions than those conditioned on entangled ones. From this, we construct our metric using the aggregate topological similarity across data submanifolds conditioned on every latent dimension in the generative model.

In this paper, we make several key contributions:

- We present an unsupervised metric for evaluating disentanglement that only requires the generative model (decoder) and is dataset-agnostic. In order to achieve this, we propose measuring the topology of the learned data manifold with respect to its latent dimensions. Our metric accounts for topological similarity across homeomorphic dimensions.
- We also introduce a supervised variant that compares the generated topology to a real reference.
- For both variants, we develop a topological similarity criterion based on Wasserstein distance, which defines a metric on barcode space in persistent homology.
- Empirically, we perform an extensive set of experiments to demonstrate the applicability of our method across 10 models and three datasets using both the supervised and unsupervised variants. We find that our results are consistent with several existing methods.

2 BACKGROUND

Our method draws inspiration from the Manifold Hypothesis (Cayton, 2005; Narayanan and Mitter, 2010; Goodfellow et al., 2016), which posits that there exists a low-dimensional manifold $\mathcal{M}_{\text{data}}$ on which real data lie and $p_{\text{data}}(\mathbf{x})$ is supported, and that generative models $g : Z \rightarrow X$ learn an approximation of that manifold $\mathcal{M}_{\text{model}}$. As a result, the true data manifold $\mathcal{M}_{\text{data}}$ contains high-density regions, separated by large expanses of low-density regions, assuming a topology. $\mathcal{M}_{\text{model}}$ approximates this topology through the learning process.

A k -manifold is a space X , for example a subset of \mathbb{R}^n for some n , so that for every point $x \in X$, there is a subset which can be reparametrized to an open disc in \mathbb{R}^k . A *coordinate chart* for the manifold X is an open subset U of \mathbb{R}^k together with a continuous parametrization $g : U \rightarrow X$ of a subset of X . An *atlas* for X is a collection of coordinate charts that cover X . For example, any open hemisphere in a sphere is a coordinate chart., and the collection of all open hemispheres form an atlas. We say two manifolds are *homeomorphic* if there is a continuous map from X to Y that has a continuous inverse. Intuitively, two manifolds are homeomorphic if one can be viewed as a continuous reparametrization of the other. If we have a continuous map f from a manifold X to \mathbb{R}^n , and are given two nearby points \vec{x} and \vec{y} in \mathbb{R}^n , it is often useful to compare the subsets $f^{-1}(\vec{x})$ and $f^{-1}(\vec{y})$, which are manifolds (where the Jacobian matrix of f is maximal rank). They are frequently homeomorphic, and we will be using topological invariants that can distinguish between two non-homeomorphic manifolds.

Among the easiest topological invariants to numerically estimate is homology (Hatcher, 2005), which characterizes the number of k -dimensional holes in a topological space such as a manifold. Intuitively, these holes correspond to low-density regions on the manifold. The field of persistent homology offers several methods for estimating the homology of a topological space from data samples (Carlsson, 2019). Under the manifold hypothesis, the latent space of a deep generative model

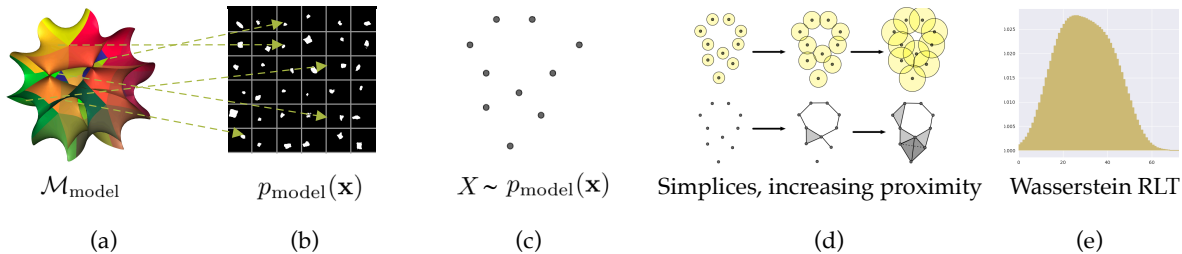


Figure 2: Illustration of obtaining Wasserstein Relative Living Times (W. RLTs) from a manifold. (a) a learned manifold with holes, on which (b) $p_{\text{model}}(\mathbf{x})$ is presumed to be supported (images here are generated *dSprites*). From $p_{\text{model}}(\mathbf{x})$, we obtain (c) samples X . From X , we construct (d) simplicial complexes from increasing the proximity of balls over time, producing a distribution of holes across varying dimensionalities, or an RLT. In this example, we first have no holes in the simplicial complex (homology group H_0), then both a 1-dimensional hole and no hole (H_1, H_0), and finally only a 1-dimensional hole (H_1). Finding the W. barycenter of several RLTs, we obtain (e) a W. RLT. Figure (a) is drawn from Hanson (1994) and (c) and (d) are drawn from Khrulkov and Oseledets (2018).

has an extremely dense underlying manifold with few, if any, holes, making homology difficult to measure and distinguish across submanifolds. As a result, recent work on Relative Living Times (RLTs) (Khrulkov and Oseledets, 2018) has used persistent homology to estimate a model’s topology on its data manifold, also enabling the direct comparison of generated data manifolds to real ones. For low-dimensional data (and images), points correspond to their vector representation (flattened matrices of pixels); for high-dimensional data, particularly images, points correspond to vectorized embeddings extracted from a pretrained VGG16 (Simonyan and Zisserman, 2015).

To obtain RLTs, we first construct a family of simplicial complexes—graph-like structures—from data samples, each starting with a set of vertices representing the data points and no edges (Figure 2). These are *Vietoris-Rips complexes* that characterize the topology of a set of points, a common method for statistically estimating topology in persistent homology (Carlsson, 2019; Lim et al., 2020). These simplicial complexes approximate the topology of the data manifold by identifying k -dimensional holes present in the simplices at varying levels of *proximity*. Proximity is defined as the radius of a ball around each symplectic vertex. If the balls of two vertices intersect, an edge is drawn between them. As proximity increases, complexes form with varying numbers of k -dimensional holes.

RLTs use the notion of increasing proximity over time to construct a discrete distribution—known as a persistence barcode (Carlsson, 2019; Zomorodian and Carlsson, 2005; Ghrist, 2008)—over the duration of each k -dimensional hole as it appears and disappears, or their lifetime relative to other holes. This is merely one method to (partially) vectorize persistence barcodes efficiently, and we leave it to future work to explore alternate methods (Adcock et al., 2013; Bubenik, 2015). To measure the topological similarity between data samples representing two generative model manifolds, Khrulkov and Oseledets (2018) then take the Euclidean mean of several RLTs to produce a discrete probability distribution, called a Mean Relative Living Time; they propose employing the Euclidean distance between two Mean Relative Living Times as the measure of topological similarity between two sets of data samples, known as the *Geometry Score*. Additional background is in Appendix B.

3 MANIFOLD INTERPRETATION OF DISENTANGLEMENT

We use prevailing definitions disentanglement where a disentangled model has a factorized latent space corresponding bijectively to factors of variation (Shu et al., 2019; Higgins et al., 2018; Duan et al., 2020). We frame our approach primarily on the definition in Shu et al. (2019), with a more formal connection between their approach and our method in Appendix A.

From the manifold perspective, disentanglement is an extrinsic property that is dependent on the generative model’s atlas. Consider a disentangled generative model g with manifold \mathcal{M} that assumes topology τ . We can define another generative model g' with the same underlying manifold \mathcal{M} and τ , but it is entangled and has a different atlas. In fact, we can define several alternate disentangled and

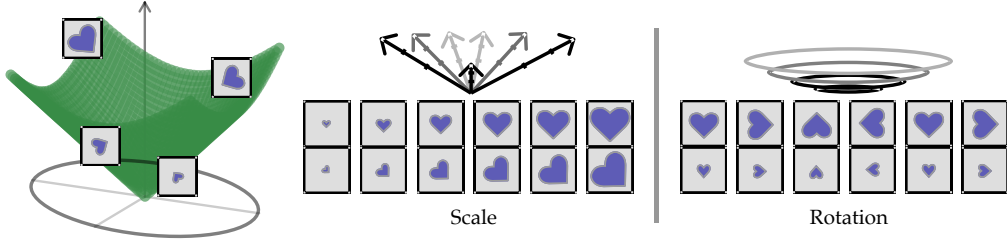


Figure 3: Consider a set of images of a spinning heart with different sizes. We can embed these images on any group that combines a rotational and a scalar invariance (i.e. a group with the $SO(2,1)$ symmetry), visualizing this as a conical shell. The submanifolds corresponding to a given rotation have no holes, while those corresponding to scale have a 1D hole. Notably, the topology of the submanifold when holding scale fixed is different from the topology when holding rotation fixed. Latent dimensions of a disentangled model would embed images on each axis. By contrast, an entangled model may embed one dimension on an axis and the other in a spiral.

entangled atlases, provided there are multiple valid factorizations of the space. As a result, we need a method that can detect whether an atlas is disentangled.

In this paper, we slice \mathcal{M} into submanifolds $U_{s_i=v} \subset \mathcal{M}$ that are conditioned on a factor s_i at value v . These conditional submanifolds have separate topologies from \mathcal{M} and depend on the coordinate chart ϕ_i associating it with the model’s atlas. If we observe samples from one factor, e.g. $X_{s_1=v} \sim U_{s_1=v}$ at varying values of v , we find that all samples $X_{s_1=v}$ appear identical, except with respect to that single factor of variation s_i set to a different value of v . For a generative model, the correspondence between latent dimensions z_j and factors s_i is not known upfront. As a result, we perform this procedure by conditioning on each latent dimension z_j .

Conditional submanifold topology. For two submanifolds to have the same topology, there needs to be a continuous and invertible mapping between them. First, assume that there exists an invertible mapping, or encoder $e : X \rightarrow Z$, and a generative model $g : Z \rightarrow X$, where both functions are continuous. Then, for a given \mathbf{z} and $\mathbf{x} = g(\mathbf{z})$, we can recover \mathbf{z} by composition $\mathbf{z} = e(g(\mathbf{z}))$. We can also construct a simple linear mapping $l : \mathbf{z} \rightarrow \mathbf{z}'$, which adapts a factor’s value, such that $\mathbf{z}' = l(e(g(\mathbf{z})))$ remains continuously deformable. This holds across factors, where the manifold is topologically symmetric with respect to different factors, i.e. its conditional submanifolds are homeomorphic. As an example, consider a disentangled generative model $g(z_0, z_1, z_2)$ that traces a tri-axial ellipsoid $\frac{x^2}{z_0^2} + \frac{y^2}{z_1^2} + \frac{z^2}{z_2^2} = 1$. If we condition the model on varying values of each factor, the resulting submanifolds are ellipses and have the same topology.

Most complex manifolds have submanifolds that have non-homeomorphic factors of variation. For example, consider a generative model $g(z_0, z_1)$ that traces a cylindrical shell with angle z_0 , height z_1 , and for simplicity, no thickness. The submanifolds conditioned on angle z_0 form lines (no holes), while the submanifolds conditioned on height z_1 form circles (a 1D hole). However, the topology remains the same for a given factor. A visualization of this principle on a cone is shown in Figure 3. Taken together, this means that submanifolds within a factor (intra-factor) are homeomorphic, while submanifolds between factors (extra-factor) can be either homeomorphic or non-homeomorphic.

Topological asymmetry. Because topologically asymmetric submanifolds are non-homeomorphic, using a single e that continuously deforms across submanifolds no longer holds under disentanglement. To address this, assume that for each factor j , there exists a continuous invertible encoder $e_j : X \rightarrow Z_j$ that exclusively encodes information on j from a generated sample. In the cylindrical shell example, this means continuously deforming across submanifolds conditioned on varying values of z_0 using e_0 (deforming between lines) and likewise for z_1 using an e_1 (deforming between circles). Note that this formulation prevents continuous deformations between lines and circles. More generally, we cannot continuously deform across submanifolds conditioned by arbitrary factors and expect the topology to be preserved. This procedure now amounts to performing latent traversals along an axis and observing the topology of the resulting submanifolds. In a disentangled model, the j -conditional submanifolds exhibit the same topology by continuous composition of $\mathbf{z} = e_j(g(\mathbf{z}))$, using a linear mapping that only adapts factor j across the traversal, i.e. $\mathbf{z}' = l_j(e_j(g(\mathbf{z})))$.

In an entangled model by contrast, more than one factor—such as both the angle and height in the cylindrical shell example—exhibit variation along a dimension z_j . Put another way, the topology on submanifolds conditioned on z_j changes when multiple factors contribute to variation along this dimension. Concretely, following the cylindrical shell example, a dimension that encodes height and, after a certain height threshold, also begins to adapt the angle will result in a topology that changes at that threshold to include a 2D hole. Consequently, submanifolds conditioned on the same factor z_j have the same topology in a disentangled model, yet different topology in an entangled one.

Because we cannot assume that the data manifold of a generative model is completely symmetric, we only consider submanifolds to be homeomorphic along the same factor in a disentangled model. By contrast, since these submanifolds are not homeomorphic in an entangled model, we can measure the similarity across these submanifolds to evaluate a model’s disentanglement. Using this notion of intra-factor topological similarity, we may sufficiently measure disentanglement in most cases, but it does not shield us from the scenario where a generative model learns a single trivial factor along all dimensions, i.e. a factorization of one. If we assume that there exists asymmetries in the data manifold, then ensuring that the manifold exhibits topological *dissimilarity* between certain factors would disarm that case. We operationalize this by identifying homeomorphic groups of factors, whereby each group has its own distinct topology to ensure there is not a factorization of one. Within groups, we measure topological similarity, but between different groups, we calculate topological dissimilarity. Consequently, topological similarity and dissimilarity form the basis of our metric. A more principled treatment of how manifold topology measures disentanglement is in Appendix A.

3.1 TOPOLOGICAL SIMILARITY USING WASSERSTEIN RELATIVE LIVING TIMES

In order to estimate the topological similarity between conditional submanifolds, we build on Relative Living Times (Khrulkov and Oseledets, 2018) and introduce Wasserstein (W.) Relative Living Times. Wasserstein distance, unlike Euclidean distance, defines a metric on barcode space; recall that barcodes are the discrete distributions representing the presence and absence of different k -dimensional holes (or more formally known as the Betti numbers, or k -th homology groups), which are vectorized to form RLTs (Carlsson, 2019). This strongly motivates us to consider Wasserstein over Euclidean distance, which we find empirically to improve separation between distinct factors of variation (on a real disentangling dataset), with details in Appendix C. Thus, in lieu of the Euclidean mean across RLTs, we equivalently employ the W. barycenter (Agueh and Carlier, 2011). For distances between W. barycenters, we employ standard W. distance.

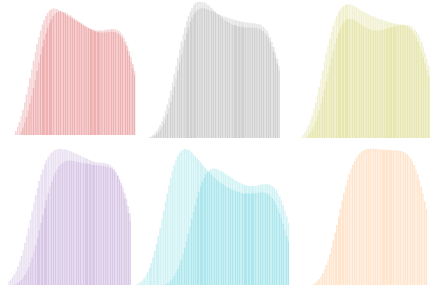


Figure 4: Wasserstein RLTs from factors in the *CelebA* dataset. Factors that are homeomorphic to each other are shown on top, and factors that are not homeomorphic to each other are shown below. Additional examples are in Appendix D.

The W. barycenter \bar{p}_w of the distributions $p_1 \dots p_N$ corresponds to finding the minimum cost for transporting \bar{p}_w to each p_i , where cost is defined in W-2 distance: $\bar{p}_w = \arg \min_q \sum_{j=1}^N \lambda_j W_2^2(q, p_j)$, where $\lambda \geq 0$ and $\sum_{j=1}^N \lambda_j = 1$. This is a weighted Fréchet mean, $\bar{p} = \arg \min_q \sum_{j=1}^N \lambda_j d(q, p_j)$, where $d = W_2^2$. In contrast, Euclidean distance, or the l_2 norm, is defined using $d = \|\cdot\|_2^2$.

Because our distributions represent discrete unnormalized counts of k -dimensional holes, we leverage recent work in unbalanced optimal transport (Chizat et al., 2018; Frogner et al., 2015) that assumes that p_i are not normalized probabilities containing varying cumulative mass. The unbalanced W. barycenter modifies the W. distance to penalize the marginal distributions based on the extended KL divergence (Chizat et al., 2018; Dognin et al., 2019). Unlike Euclidean, Hellinger, or total variation distance, W. distance defines a valid metric on barcode space in persistent homology.

We show in Appendix C that the use of both W. RLTs and W. distance result in a distance metric on sets of RLTs that best separates similar and dissimilar topologies.

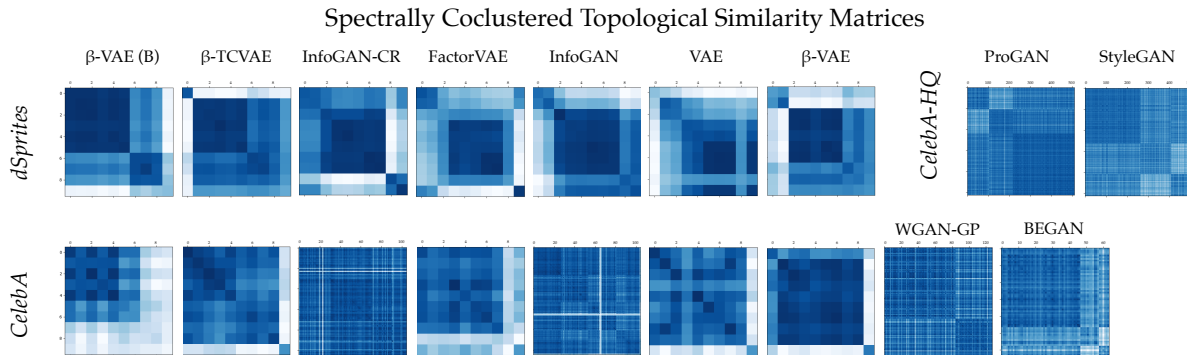


Figure 5: Topological similarity matrices across experimental conditions. Dark clusters along the diagonal indicate homeomorphic groups. Darker values indicate greater similarity (lower W . distance) to each other. Note that models spectrally cocluster differently across dataset settings.

3.2 METRIC

Equipped with a procedure for measuring topological similarity, we develop a metric for scoring the disentanglement from intra-group topological similarity and extra-group topological dissimilarity.

Beginning with intra-factor topological similarity, we are concerned with the degree to which the topology of $p_{\text{model}}(\mathbf{x}|s_i = v)$ varies with respect to a factor s_i at different values of v . Specifically, we condition the manifold on a particular factor s_i at value v , while allowing other factors $s_{\setminus i}$ to vary. We then measure the topology of this conditional submanifold. For each factor s_i , we find the topology of conditional submanifolds at varying values of v . A disentangled model would exhibit topological similarity within the set of submanifolds conditioned on the same s_i . We visualize similar and dissimilar W . RLTs on factors of the *CelebA* dataset in Figure 9.

For a generative model, the correspondence between latent dimensions z_j and factors s_i is not known upfront. As a result, we perform this procedure by conditioning on each latent dimension z_j . We then assess pairwise topological similarity across latent dimensions $\forall_{j,k} \delta(z_j, z_k)$, using W . distance between W . RLTs. This operation constructs a j -dimensional similarity matrix M . We use spectral coclustering (Dhillon, 2001) on M to cocluster z_j into ξ biclusters, which represent different groups of homeomorphic factors. Spectral coclustering uses SVD to identify, in our case, the $\xi \leq j$ most likely biclusters, or the subsets of rows that are most similar to columns in M . The resulting biclusters create a correspondence from latent dimensions z_i to a group of homeomorphic factors h_ξ . Aggregating biclusters in M , we obtain a ξ -dimensional matrix M'_ξ (see examples in Figure 5). We then minimize the total variation of intra-group variance and extra-group variance on M'_ξ to find the value for ξ . Using M'_ξ , we compute a score μ that rewards high intra-group similarity $\rho_\xi = \text{tr}(M')$ and low extra-group similarity $\rho_{\setminus \xi} = \sum_{a,b} M'_{ab} - \text{tr}(M')$. This score is based on the normalized cut objective in spectral coclustering to measure the strength of associations within a bicluster (Dhillon, 2001). As a result, the unsupervised metric $\mu = \max_{\xi \in [1,j]} \sum_{\xi} (\rho_\xi - \rho_{\setminus \xi})$.

Supervised variant. In order to capture the correspondence between the learned and real data topology, we present a supervised variant that uses labels of relevant factors on the real dataset to represent the real data topology. This is motivated in large part by F. Locatello et al. (2019), who importantly show that learning a fully disentangled a model requires supervision; further discussion is in Appendix B. While this supervised variant requires labeled data, there are no external ad-hoc classifiers or encoders that might favor one training criterion over another. The real topology is approximated in the same way as the generated, but we have desired groups of factors s_i upfront. See Figure 1 for a comparison between real and generated Wasserstein RLTs of two *dSprites* factors. Note that s_i do not necessarily need to belong to different homology groups; we account for this during spectral coclustering with the generated data manifold. The major difference is that the generated data topology is no longer compared to itself, but to the real data topology, where topological similarity is now computed between the two manifolds: $\forall_{i,j} \delta(z_j, s_i)$. Note that the relevant factors in the real topology form a specific factorization, so a model that finds an alternate factorization and that scores well on the unsupervised metric may not fare well on the supervised variant.

Model	Dataset	μ	μ_{SUP}	Model	Dataset	μ	μ_{SUP}
β -VAE _B	dSprites	23.53 ± 8.14	3.55 ± 4.25	β -VAE _B	CelebA	4.73 ± 2.27	0.29 ± 0.25
β -TCVAE	dSprites	14.92 ± 3.46	-0.79 ± 1.35	β -TCVAE	CelebA	10.66 ± 2.48	0.04 ± 0.36
InfoGAN-CR	dSprites	9.73 ± 4.03	1.85 ± 2.63	InfoGAN-CR	CelebA	0.72 ± 0.27	0.07 ± 0.15
FactorVAE	dSprites	8.66 ± 1.83	0.35 ± 0.90	FactorVAE	CelebA	8.53 ± 4.53	-0.14 ± 0.28
InfoGAN	dSprites	7.42 ± 1.19	0.16 ± 0.92	InfoGAN	CelebA	1.11 ± 0.81	0.00 ± 0.01
VAE	dSprites	7.05 ± 1.25	1.54 ± 1.27	VAE	CelebA	6.98 ± 2.78	0.00 ± 0.15
β -VAE	dSprites	6.53 ± 2.89	1.81 ± 2.90	β -VAE	CelebA	15.10 ± 8.94	0.13 ± 0.38
StyleGAN	CelebA-HQ	1.03 ± 0.24	0.77 ± 0.07	BEGAN	CelebA	0.85 ± 0.25	0.22 ± 0.10
ProGAN	CelebA-HQ	0.68 ± 0.08	0.37 ± 0.45	WGAN-GP	CelebA	0.83 ± 0.29	0.07 ± 0.13

Table 1: Experimental results on several generative models and dataset settings for our unsupervised μ and supervised μ_{SUP} metrics, across five runs. We find that, consistent with other disentanglement metrics, no model architecture that we evaluated supercedes all others on every metric and dataset.

We use the same spectral coclustering procedure, though this time on a $j \times i$ matrix. Note that because it is not a square matrix, $\rho_\xi = \sum_{a=0}^{\xi} M'_{aa}$ and $\rho_{\setminus\xi} = \sum_{a=0}^{\xi} \sum_{b=0}^{\xi} M'_{ab} - \rho_\xi$, where $\xi = \min(\xi, i)$ so that we only consider the real factors if $\xi > i$. Finally, we normalize the final score by the number of factors $\mu_{\text{SUP}} = \mu/i$, to penalize methods that do not find any correspondence to some factors. Ultimately, the supervised score favors groups of latent factors that have similar topological submanifolds to those of the reals.

Limitations. In Figure 6, we highlight cases where our metric may face limitations, delineated from scenarios where it would behave as expected. The first limitation is that it is theoretically possible for two factors to be disentangled and, under cases of complete symmetry, still have the same topology. This is more likely in datasets with trivial topologies that are significantly simpler than *dSprites*. While partial symmetry is handled in the metric with spectral coclustering of homeomorphic factors, complete symmetry is not.

Because we assume that the manifold is not exactly symmetric, we do not account for all factors to present symmetry. In order to safeguard against this case, we would need to consider the covariance of topological similarities across pairwise conditional manifolds. This requires selecting fixed points from v that hold two dimensions constant, and subsequently verifying that the topologies do not covary. However, this approach comes with a high computational cost for a benefit only to, for the most part, simple toy datasets. If we assign a Dirichlet process prior over all possible topologies (Ranganathan, 2008) and treat the number of factors as the number of samples, we find that the probability of having only a single set of all homeomorphic factors decreases factorially with the number of dimensions n .

An additional limitation of our method is that RLTs do not compute a full topology of the data manifold, but instead efficiently approximate one topological invariant, homology, so that we can comparatively rank generative models on disentanglement. Our overall approach of measuring disentanglement is general enough to incorporate measurements of other topological invariants.

4 EXPERIMENTS

Across an extensive set of experiments, our goal is to show the extent to which our metric is able to evaluate across different generative model architectures, training criteria, and datasets. We additionally show that our metric performs similarly to existing disentanglement metrics, without the same architectural or dataset-specific needs. Additional training details are in Appendix G.

Datasets. We present empirical results on three datasets: (1) *dSprites* (Matthey et al., 2017) is a canonical disentanglement dataset whose five generating factors {shape, scale, orientation, x-position, y-position} are complete and independent, i.e. they fully describe all combinations in the dataset;

	Similar Topology	Different Topology
Entangled	Expected Low score τ	Not applicable under the manifold interpretation
Disentangled	Unlikely in complex data manifolds	Expected High score τ

Figure 6: Topology-entanglement combinations considered in our method.

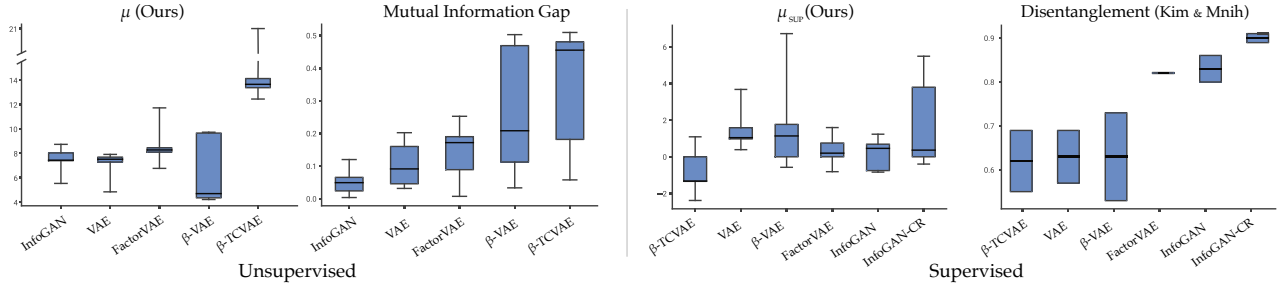


Figure 7: Comparisons of μ to MIG (Chen et al., 2018b) and μ_{SUP} to classifier-based disentanglement score (Kim and Mnih, 2018).

(2) *CelebA* is a popular dataset for disentanglement and image generation, and is comprised of over 202K human faces, which we align and crop to be 64×64 px (Liu et al., 2015). There are also 40 attribute labels for each image; and (3) *CelebA-HQ*, a higher resolution subset of *CelebA* consisting of 30K images (Karras et al., 2018).

Generative models. We compare ten canonical generative models, including a standard VAE, β -VAE (Higgins et al., 2017), β -VAE_B (Burgess et al., 2018), FactorVAE (Kim and Mnih, 2018), β -TCVAE (Chen et al., 2018b), InfoGAN (Chen et al., 2016), InfoGAN-CR (Lin et al., 2020), BEGAN (Berthelot et al., 2017), WGAN-GP (Gulrajani et al., 2017), ProGAN (Karras et al., 2018), and StyleGAN (Karras et al., 2019). We evaluate VAE and InfoGAN variants on dSprites and *CelebA*, WGAN-GP and BEGAN on *CelebA*, and ProGAN and StyleGAN on *CelebA-HQ*. We match models to datasets, on which they have previously demonstrated strong performance and stable training.

Metric parity. We find that $\{\mu, \mu_{\text{SUP}}\}$ rank models similarly to several other frequently cited metrics, including: (1) an information-theoretic metric MIG that uses an encoder (Chen et al., 2018b), (2) a supervised metric from (Kim and Mnih, 2018) that uses a classifier, and (3) a dataset-specific metric PPL (Karras et al., 2019) that caters to face datasets such as *CelebA-HQ*. We use scores from their respective papers and prior work (Chen et al., 2018b; Kim and Mnih, 2018; Lin et al., 2020; Karras et al., 2019) to show that our method ranks most or all models the same across each metric (μ compared to MIG and PPL, μ_{SUP} to the supervised method). The source of deviation from MIG is the ranking of β -VAE; nevertheless, both of our scores exhibit exceptionally high variance across runs, suggesting that β -VAE has inconsistent disentanglement performance (see Figure 7). The classifier method ranks β -TCVAE and FactorVAE quite far apart, while ours ranks them similarly. We find that their nearly identical training objectives should rank them more closely and do not find this disparity particularly unexpected. Finally, our method agrees with PPL rankings on *CelebA-HQ*.

As shown in Table 1, these experiments highlight several key observations:

- Performance is not only architecture-dependent, but also dataset-dependent. This highlights the importance of having a metric that can cater to comparisons across these facets. Nevertheless, we note that β -VAE_B shows especially strong results on both metrics and two dataset settings.
- As expected, the VAE and InfoGAN variants designed for disentanglement show greater performance on μ than their GAN counterparts. However, on μ_{SUP} , we find that BEGAN is able to perform inseparably close to β -VAE_B, suggesting that the model learns dependent factors consistent with the attributes in *CelebA*.
- With similar training objectives, β -TCVAE and FactorVAE demonstrate comparable strong performances on μ across both dSprites and *CelebA*. β -TCVAE displays slight, yet consistent, improvements over FactorVAE, which may point to FactorVAE’s underestimation of total correlation (Chen et al., 2018b). Nevertheless, FactorVAE demonstrates higher μ_{SUP} on dSprites.
- StyleGAN demonstrates consistently higher disentanglement, compared to ProGAN, which supports architectural decisions made for StyleGAN (Karras et al., 2019).

5 CONCLUSION

In this paper, we have introduced a disentanglement metric that measures intrinsic properties of a generative model with respect to its factors of variation. Our metric circumvents the typical requirements of existing metrics, such as requiring an ad-hoc model, a particular dataset, or a canonical factorization. This opens up the stage for broader comparisons across models and datasets. Our contributions also consider several cases of disentanglement, where labeled data is not available (unsupervised) or where direct comparisons to user-specified, semantically interpretable factors are desired (supervised). Ultimately, this work advances our ability to leverage the intrinsic properties of generative models to observe additional desirable facets and to apply these properties to important outstanding problems in the field.

REFERENCES

- A. Adcock, E. Carlsson, and G. Carlsson. The ring of algebraic functions on persistence bar codes. *Homology, Homotopy and Applications*, 18, 04 2013.
- M. Agueh and G. Carlier. Barycenters in the wasserstein space. *SIAM Journal on Mathematical Analysis*, 43(2):904–924, 2011.
- A. Alemi, I. Fischer, J. Dillon, and K. Murphy. Deep variational information bottleneck. In *ICLR*, 2017. URL <https://arxiv.org/abs/1612.00410>.
- Y. Bengio, A. Courville, and P. Vincent. Representation learning: A review and new perspectives. *IEEE transactions on pattern analysis and machine intelligence*, 35(8):1798–1828, 2013.
- D. Berthelot, T. Schumm, and L. Metz. Began: boundary equilibrium generative adversarial networks. *arXiv preprint arXiv:1703.10717*, 2017.
- P. Bubenik. Statistical topological data analysis using persistence landscapes. *The Journal of Machine Learning Research*, 16(1):77–102, 2015.
- C. P. Burgess, I. Higgins, A. Pal, L. Matthey, N. Watters, G. Desjardins, and A. Lerchner. Understanding disentangling in beta-vae. *arXiv preprint arXiv:1804.03599*, 2018.
- G. Carlsson. Persistent homology and applied homotopy theory. *Handbook of Homotopy Theory*, 2019.
- L. Cayton. Algorithms for manifold learning. *Univ. of California at San Diego Tech. Rep*, 12(1-17):1, 2005.
- N. Chen, A. Klushyn, R. Kurle, X. Jiang, J. Bayer, and P. van der Smagt. Metrics for deep generative models. *PMLR*, 2018a.
- T. Q. Chen, X. Li, R. B. Grosse, and D. K. Duvenaud. Isolating sources of disentanglement in variational autoencoders. In *Advances in Neural Information Processing Systems*, pages 2610–2620, 2018b.
- X. Chen, Y. Duan, R. Houthoofd, J. Schulman, I. Sutskever, and P. Abbeel. Infogan: Interpretable representation learning by information maximizing generative adversarial nets. In *Advances in neural information processing systems*, pages 2172–2180, 2016.
- L. Chizat, G. Peyré, B. Schmitzer, and F.-X. Vialard. Scaling algorithms for unbalanced optimal transport problems. *Mathematics of Computation*, 87(314):2563–2609, 2018.
- I. S. Dhillon. Co-clustering documents and words using bipartite spectral graph partitioning. In *Proceedings of the seventh ACM SIGKDD international conference on Knowledge discovery and data mining*, pages 269–274, 2001.
- P. Dognin, I. Melnyk, Y. Mroueh, J. Ross, C. D. Santos, and T. Sercu. Wasserstein barycenter model ensembling. *ICLR*, 2019.

-
- S. Duan, L. Matthey, A. Saraiva, N. Watters, C. P. Burgess, A. Lerchner, and I. Higgins. Unsupervised model selection for variational disentangled representation learning. *ICLR*, 2020.
- C. Eastwood and C. K. Williams. A framework for the quantitative evaluation of disentangled representations. *ICLR*, 2018.
- F. Locatello et al. Challenging common assumptions in the unsupervised learning of disentangled representations. *ICML*, 2019.
- C. Frogner, C. Zhang, H. Mobahi, M. Araya, and T. A. Poggio. Learning with a wasserstein loss. In *Advances in Neural Information Processing Systems*, pages 2053–2061, 2015.
- R. Ghrist. Barcodes: the persistent topology of data. *Bulletin of the American Mathematical Society*, 45(1):61–75, 2008.
- X. Glorot, A. Bordes, and Y. Bengio. Domain adaptation for large-scale sentiment classification: A deep learning approach. *ICML*, 2011.
- I. Goodfellow, Y. Bengio, and A. Courville. *Deep learning*. MIT press, 2016.
- W. Grathwohl and A. Wilson. Disentangling space and time in video with hierarchical variational auto-encoders. *arXiv preprint arXiv:1612.04440*, 2016.
- I. Gulrajani, F. Ahmed, M. Arjovsky, V. Dumoulin, and A. C. Courville. Improved training of wasserstein gans. In *Advances in Neural Information Processing Systems*, pages 5767–5777, 2017.
- A. J. Hanson. A construction for computer visualization of certain complex curves. *Notices of the Amer. Math. Soc*, 41(9):1156–1163, 1994.
- A. Hatcher. *Algebraic topology*. Cambridge University Press, 2005.
- I. Higgins, L. Matthey, A. Pal, C. Burgess, X. Glorot, M. Botvinick, S. Mohamed, and A. Lerchner. beta-vae: Learning basic visual concepts with a constrained variational framework. *ICLR*, 2(5):6, 2017.
- I. Higgins, D. Amos, D. Pfau, S. Racaniere, L. Matthey, D. Rezende, and A. Lerchner. Towards a definition of disentangled representations. *arXiv preprint arXiv:1812.02230*, 2018.
- D. Horak, S. Yu, and G. Salimi-Khorshidi. Topology distance: A topology-based approach for evaluating generative adversarial networks. *arXiv preprint arXiv:2002.12054*, 2020.
- T. Karaletsos, S. Belongie, and G. Rätsch. Bayesian representation learning with oracle constraints. *ICLR*, 2015.
- T. Karras, T. Aila, S. Laine, and J. Lehtinen. Progressive growing of gans for improved quality, stability, and variation. *ICLR*, 2018.
- T. Karras, S. Laine, and T. Aila. A style-based generator architecture for generative adversarial networks. *CVPR*, 2019.
- V. Khruikov and I. Oseledets. Geometry score: A method for comparing generative adversarial networks. *ICML*, 2018.
- H. Kim and A. Mnih. Disentangling by factorising. *PMLR*, 2018.
- S. Lim, F. Memoli, and O. B. Okutan. Vietoris-rips persistent homology, injective metric spaces, and the filling radius. *arXiv preprint arXiv:2001.07588*, 2020.
- Z. Lin, K. K. Thekumparampil, G. Fanti, and S. Oh. Infogan-cr: Disentangling generative adversarial networks with contrastive regularizers. *ICML*, 2020.
- Z. Liu, P. Luo, X. Wang, and X. Tang. Deep learning face attributes in the wild. In *Proceedings of International Conference on Computer Vision (ICCV)*, 2015.
- M. Vlachos et al. Improving co-cluster quality with application to product recommendations. *CIKM*, 2014.

-
- L. Matthey, I. Higgins, D. Hassabis, and A. Lerchner. dsprites: Disentanglement testing sprites dataset. <https://github.com/deepmind/dsprites-dataset/>, 2017.
- H. Narayanan and S. Mitter. Sample complexity of testing the manifold hypothesis. In *Advances in neural information processing systems*, pages 1786–1794, 2010.
- F. Pedregosa, G. Varoquaux, A. Gramfort, V. Michel, B. Thirion, O. Grisel, M. Blondel, P. Prettenhofer, R. Weiss, V. Dubourg, J. Vanderplas, A. Passos, D. Cournapeau, M. Brucher, M. Perrot, and E. Duchesnay. Scikit-learn: Machine learning in Python. *Journal of Machine Learning Research*, 12:2825–2830, 2011.
- A. Ranganathan. *Probabilistic topological maps*. PhD thesis, Georgia Institute of Technology, 2008.
- K. Ridgeway. A survey of inductive biases for factorial representation-learning. *CoRR abs/1612.05299*, 2016.
- B. Rieck, M. Togninalli, C. Bock, M. Moor, M. Horn, T. Gumbsch, and K. Borgwardt. Neural persistence: A complexity measure for deep neural networks using algebraic topology. *ICLR 2019*, 2018.
- H. Shao, A. Kumar, and P. Thomas Fletcher. The riemannian geometry of deep generative models. In *Proceedings of the IEEE Conference on Computer Vision and Pattern Recognition Workshops*, pages 315–323, 2018.
- R. Shu, Y. Chen, A. Kumar, S. Ermon, and B. Poole. Weakly supervised disentanglement with guarantees. *ICLR 2020*, 2019.
- A. Shukla, S. Uppal, S. Bhagat, S. Anand, and P. Turaga. Geometry of deep generative models for disentangled representations. In *Proceedings of the 11th Indian Conference on Computer Vision, Graphics and Image Processing*, pages 1–8, 2018.
- K. Simonyan and A. Zisserman. Very deep convolutional networks for large-scale image recognition. In Y. Bengio and Y. LeCun, editors, *3rd International Conference on Learning Representations, ICLR 2015, San Diego, CA, USA, May 7-9, 2015, Conference Track Proceedings*, 2015. URL <http://arxiv.org/abs/1409.1556>.
- D. Stutz, M. Hein, and B. Schiele. Disentangling adversarial robustness and generalization. In *Proceedings of the IEEE Conference on Computer Vision and Pattern Recognition*, pages 6976–6987, 2019.
- T. Lin et al. On efficient optimal transport: An analysis of greedy and accelerated mirror descent algorithms. *ICML*, 2019.
- A. Zomorodian and G. Carlsson. Computing persistent homology. *Discrete & Computational Geometry*, 33(2):249–274, 2005.

APPENDIX A: OUR APPROACH UNDER THE DEFINITION OF DISENTANGLEMENT

Our method follows from a prior definition of disentanglement (Shu et al., 2019), which decomposes disentanglement into two components, *restrictiveness* and *consistency*. Restrictiveness over a set of latent dimensions $z_I = z_{j:k}$ is met when changes to z_I correspond to only changes to the factors of variation s_I . Consistency is met when changes to the set of factors s_I is only controlled by changes to the latent dimensions z_I . This decomposition allows for statistically dependent factors of variation s_i to exist, which is often present in naturally occurring data. For a model to be fully disentangled requires every index of the model to be disentangled.

We approach consistency and restrictiveness from measuring manifold topology. We first assume the manifold X of a generative model is equipped with an atlas $g_j : Z_j \rightarrow X$, where Z_j is an open subset of \mathbb{R}^n and n is the dimension of the manifold. Additionally, we have factors of variation $s_i : X \rightarrow \mathbb{R}^n$. We would like to drive only one of these maps s_i , while leaving the others $s_{\setminus i}$ fixed. Of course, we now have the composite maps $s_i \circ g_j : Z_j \rightarrow \mathbb{R}^n$, which can be thought of as a map from a small ball in $Z_j \in \mathbb{R}^n$ into \mathbb{R}^n . Our goal to find maps $\alpha_j : \mathbb{R}^n \rightarrow \mathbb{R}^n$ so that the map $s_i \circ g_j \circ \alpha_j$ has the form $(z_1, \dots, z_n) \rightarrow (f_1(z_1), \dots, f_n(z_n))$ and the i -th output depends only on the i -th input. Because $z_i \rightarrow f_i(z_i)$ is topologically distinct, we can use this to evaluate disentanglement.

We derive measures of failure on this diagonalization, and our idea is to study the submanifolds $(s_i \circ g_j)^{-1}(z_{\setminus i})$, in particular the persistent homology of these submanifolds, to generate an evaluation metric which is guiding us towards the disentangled situation. We believe that under a perfectly disentangled model, perturbing the value of z_i should not change the topology of the manifold $(s_i \circ g_j)^{-1}(z_i)$ (restrictiveness) or $(s_{\setminus i} \cdot g_j)^{-1}(z_{\setminus i})$ (consistency). From this, we measure disentanglement through its decomposition of consistency and restrictiveness, by comparing the persistence barcodes of these submanifolds.

We also cluster latent dimensions into groups, so our metric rewards disentangled groups, and moreover rewards maximizing the number of disentangled groups, which would be interpreted as products of tangled manifolds.

Assumptions. We make the following assumptions:

- *Assumption A.* Each map $z_i \rightarrow f_i(z_i)$ is topologically distinct.
- *Assumption B.* We can measure the persistent homology of the generated space.
- *Assumption C.* If a set of mappings $z_j \rightarrow f_j(z_j)$ are not topologically distinct, then we can treat their shared z_i or s_i dimension as the same dimension.
- *Assumption D.* In the supervised case, each s_i can be observed for each $x \in X$.

With our method, we can evaluate the degree to which a set of latent dimensions z_I corresponds to a single s_i . This is a stronger form of *restrictiveness* that disentanglement necessitates. In order to identify z_I , we cluster topologically similar latent dimensions. We *penalize intra-cluster variance*, which discourages having a set of latent dimensions z_I correspond to distinct factors of variation and which denotes higher restrictiveness.

Furthermore, we can evaluate the degree to which a single factor s_i is affected by different clusters of latent dimensions $\{z_I, z_J, \dots\}$, which also control other factors of variation. Removing shared factors increases consistency, by increasing the distance between distinct clusters. As a result, distinct clusters cannot be similar if they are consistent. This corresponds to a stronger form of *consistency* that disentanglement necessitates. Thus, we *penalize extra-cluster similarity*, which encourages topological variation between clusters and which denotes higher consistency.

Additional note on other definitions of disentanglement. As noted in a foundational paper on disentanglement (Bengio et al., 2013), disentanglement constitutes a bijective mapping between factors of variation in the data to dimensions in the latent space Z , e.g. $\forall_i \mathbf{z}_i = e(g(\mathbf{z}_i))$. Using homology, we can determine whether this bijective mapping holds along different factors, by observing the topological similarity of their conditional submanifolds and measuring the extent to which they continuously deform into each other. Aligned with newer definitions of disentanglement (Higgins et al., 2018; Duan et al., 2020), our framing permits multiple valid factorizations, where different groups of homeomorphic factors can compose alternate factorizations. Our supervised variant is meant to consider a target factorization corresponding to factors on the real manifold. In this variant,

we follow the existing definition of supervised disentanglement (Shu et al., 2019) that allows different subsets of dimensions to contribute to a target factor and for target factors to exhibit statistical dependence.

APPENDIX B: ADDITIONAL BACKGROUND

In addition to the background section of our paper, we would like to point out related work, some reiterated for ease of cohesively examining the related literature.

Disentanglement metrics. Existing disentanglement metrics depend on an external model such as an encoder or classifier to be applicable across datasets, or dataset-specific preprocessing. Several metrics train classifiers to detect separability of the data, generated by conditioning on different latent dimensions (Eastwood and Williams, 2018; Kim and Mnih, 2018; Karras et al., 2019). These are reliant on hyperparameters and the architecture of the classifiers. Recently, the mutual information gap MIG was proposed as an information-theoretic metric, yet relies on a readily available encoder in order to estimate latent entropy (Chen et al., 2018b). Many state-of-the-art GANs do not have an encoder readily available, and this has even been cited as a barrier to use (Karras et al., 2019). Finally, the perceptual path length was proposed to measure disentanglement without relying on an external model, but the method is specific to face datasets such as CelebA, as it crops out the background prior to evaluation (Karras et al., 2019). To address these limitations in a metric’s applicability and scope, we propose a method that focuses on only using the generative model’s decoder $g : \mathbb{Z} \rightarrow \mathbb{X}$ and can be applied across datasets. Additionally, because the utility of disentanglement is often with respect specific subsets of factors that are human-interpretable, we include a supervised variant of our metric that compares the real data manifold with the generated one. Finally, there is a difference between evaluating disentanglement and learning a disentangled representation, the latter of which requires constructing a valid loss function for learning and guaranteeing disentanglement, a process that requires at least weak supervision (F. Locatello et al., 2019).

Geometry of deep generative models. Prior work has explored applying Riemannian geometry to deep generative models (Shao et al., 2018; Chen et al., 2018a; Rieck et al., 2018; Horak et al., 2020). One work approximates the geodesics of the latent manifold to visually inspect deep generative models as an alternative to linear interpolation (Chen et al., 2018a). Another work also explores computing geodesics efficiently and shows that style between interpolations can be transferred with the approach (Shao et al., 2018). Horak et al. (2020) use persistent homology for comparing GAN evaluation metrics FID, KID, IS, and the geometry score from (Khrulkov and Oseledets, 2018). The closest work to ours has explored the geometry, specifically the normalized margin and tangent space alignment, of latent spaces in disentangling VAE models (Shukla et al., 2018). This work is interesting in that it leverages the lower dimensionality of latent spaces to enable more computationally feasible calculations, such as singular value decomposition. However, they do not propose an disentanglement evaluation method and do not explore the learned data manifold or homology.

Persistent homology: barcodes and Wasserstein distance. Carlsson (2019) presents a survey of persistent homology and its applied uses. Specifically, there are multiple methods for vectorizing persistence barcodes, including persistence landscapes, persistence images, symmetric polynomials (Carlsson, 2019; Bubenik, 2015; Adcock et al., 2013). Additionally, Wasserstein distance defines a metric on barcode space, as detailed by Carlsson (2019):

$$W_p(B_1, B_2) = \inf_{\theta \in \mathcal{D}(B_1, B_2)} \left(\sum_{I \in B'_1} \pi(I, \theta(I))^p \right)^{\frac{1}{p}}$$

where $p > 0$ or $p = \infty$, B_1 and B_2 are two barcodes, $\mathcal{D}(B_1, B_2)$ denotes the set of all bijections $\theta : B_1 \rightarrow B_2$ for which $\pi(I, \theta(I)) \neq 0$ for only infinitely many $I \in B'_1$, π refers to the penalty function between barcodes. Thus, we use Wasserstein distance where $p = 2$, which underlies Wasserstein barycenters, on our barcodes, over prior work using Euclidean distance and Euclidean means (Khrulkov and Oseledets, 2018).

APPENDIX C: WASSERSTEIN MEAN RLTs VS. EUCLIDEAN MEAN RLTs

We show visual comparisons of our method (Wasserstein Relative Living Times) against the prior method using the Euclidean mean to obtain the average distribution across Relative Living Times (Khrulkov and Oseledets, 2018) in Figure 8.

We empirically evaluate the use of Euclidean distance compared to W. distance and Euclidean mean compared to W. mean on the real *dSprites* dataset in Table 2. The table also indicates that the Wasserstein distance between Wasserstein barycenters is the most capable of differentiating similar and dissimilar topologies.

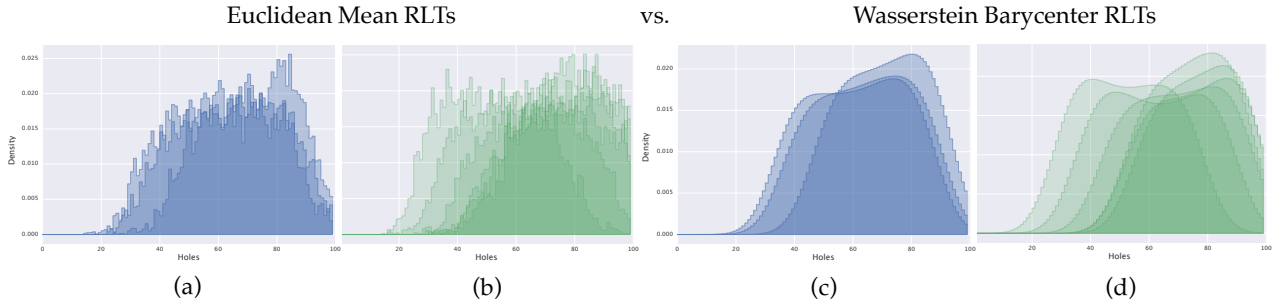


Figure 8: Comparison of each factor’s topological signatures in *dSprites* derived from the Euclidean mean on the left (a) and (b) (Khrulkov and Oseledets, 2018) to our method of deriving them from taking the Wasserstein barycenters on the right (c) and (d). Notice visually that the Euclidean mean collapses geometric information, rendering the two topological signatures (a) and (b) more indistinct, while the Wasserstein barycenters exhibit much smoother distributions and construct distinct topological signatures for each factor, (c) and (d).

RLT Distance Metric	Wasserstein RLTs	Wasserstein Distance	Difference Ratio
<i>Geometry Score</i>	–	–	1.60x
(<i>W. RLT</i>)	✓	–	1.75x
(<i>W. Distance</i>)	–	✓	2.14x
Ours	✓	✓	2.93x

Table 2: **Wasserstein distance: empirical study and ablation.** We evaluate the ratio between the mean distance between homeomorphic RLTs and non-homeomorphic RLTs with an ablation of our proposed use of W. distance and W. RLTs on real images in *dSprites*, compared to the *Geometry Score* metric proposed in Khrulkov and Oseledets (2018). A higher ratio on known factors of variation indicates a distance metric on RLTs that is better at identifying similar topologies and distinguishing different topologies.

APPENDIX D: ADDITIONAL HOMEOMORPHIC AND NON-HOMEOMORPHIC WASSERSTEIN RELATIVE LIVING TIMES

An extended figure, from Figure 4 in the main text, is shown here, illustrating that homeomorphic groups of factors based on their W. RLTs look visually similar.

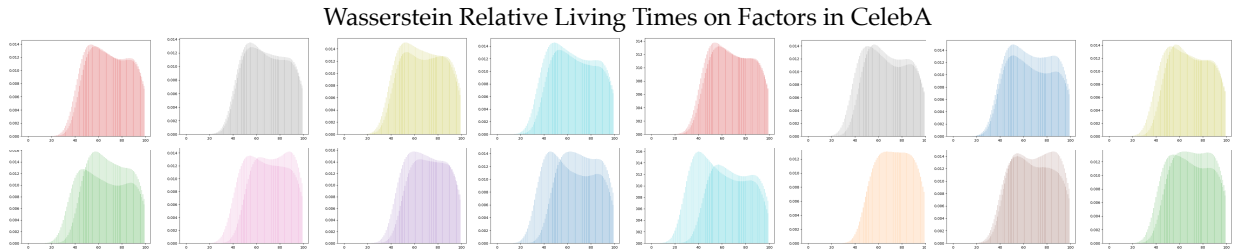


Figure 9: Additional Wasserstein RLTs from several more factors in the *CelebA* dataset. As before, factors which are homeomorphic to each other are shown on top, and factors which are not homeomorphic to each other are shown below.

APPENDIX E: TOPOLOGICAL SIGNATURES OF DSPRITES

We show topological signatures for each factor from the real *dSprites* dataset. In the supervised variant, we discover that similar topological signatures in the generated manifold match the ones in the reals for corresponding latent interpretations that semantically adapt these factors.

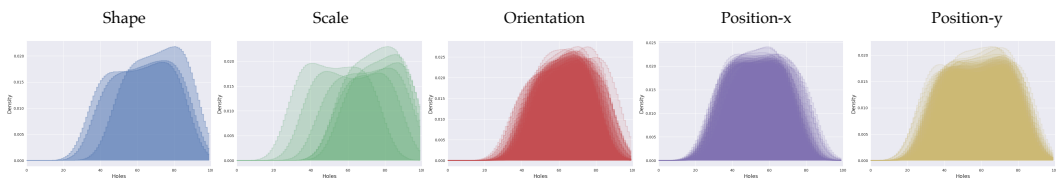


Figure 10: Topological signatures of each factor in *dSprites*. Each graph illustrates an overlay of different topological signatures (W. RLTs), produced when holding a given value of that factor constant while varying others. For example, in the first graph, the three curves indicate three shapes: ellipse, heart, and square. Notably, these sets of topological signatures present distinguishing features in aggregate.

APPENDIX F: TOPOLOGICAL SIMILARITY MATRIX OF *dSprites*

In Figure 11, we display the topological similarity matrix for the *dSprites* dataset, showing every value of each factor. A visible diagonal can be seen for each factor. Observe that the first three squares in the top left corner correspond to shape, the next six to scale, the next forty to orientation, the next thirty-six to x-position, and finally the last thirty-six to y-position. Note that this grid uses our method (W. distance) and is not spectrally coclustered.

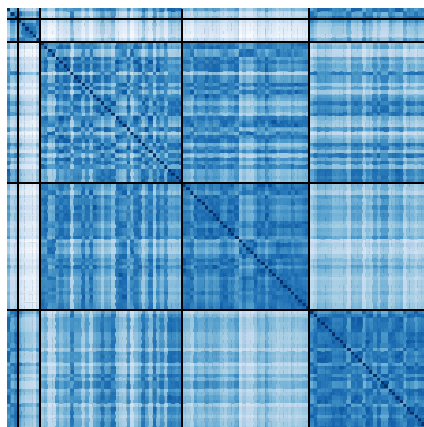


Figure 11: Topological similarity matrix on *dSprites* (reals), across values of every factor.

APPENDIX G: HYPERPARAMETERS

For all models, we used open-sourced PyTorch implementations and model checkpoints that implement prior work using default hyperparameters from the papers. We use pretrained model checkpoints and do not tune them further. One exception of using TensorFlow is the InfoGAN variants, where we could not reproduce results from any open-sourced PyTorch implementations, a known issue for InfoGAN (Higgins et al., 2017; Kim and Mnih, 2018), and instead training to the default number of epochs and hyperparameters based on the papers, because pretrained checkpoints were not available for these tasks. Additionally, we use default hyperparameters and functions for spectral co-clustering (scikit-learn, Pedregosa et al. (2011)) and Geometry Score implementations. The Geometry Score implementation used a gamma of $\frac{1}{128}$ and an n of 1000. Following the suggestion in Khrlukov and Oseledets (2018), we also used a pretrained VGG16 (Simonyan and Zisserman, 2015) as a feature extractor to embed high-dimensional images. All of these hyperparameters were constant across all datasets, models, and experiments.

APPENDIX H: COMPUTATIONAL COMPLEXITY

Let n be the number of RLTs per latent dimension, L_0 be the number of RLT landmarks, N be the number of images sampled per latent dimension, D_z be the number of latent dimensions, D_s be the number of factors of variation, and B be the number of bins for the probability distribution histogram:

- (a) Calculating the nD_z RLTs per D_z latent dimensions is $O(nD_zD_sNL_0)$ (Khrlukov and Oseledets, 2018).
- (b) Calculating D_z W. barycenters is $O(nD_zB^2m)$, with Maxiter m from Dognin et al. (2019).
- (c) Calculating W. distances between all D_z barycenters is $O(D_z^2B^2/\varepsilon^2)$ by the Sinkhorn algorithm with tolerance ε (T. Lin et al., 2019).
- (d) Spectral coclustering can be computed in $O(D_z^2)$ (M. Vlachos et al., 2014), and we optimize over the number of biclusters, of which there are at most D_z , so this is $O(D_z^3)$. Calculating the bicluster scores has the same runtime.

Treating ε and m as constants, and noting $B \leq L_0 \leq N$, then this is $O(nD_zD_sNL_0 + D_z^2B^2 + D_z^3)$. Note that many of these subprocedures can be substantially parallelized.

APPENDIX I: ETHICAL CONSIDERATIONS

This research can aid in alleviating bias in deep generative models and more generally, unsupervised learning. Disentanglement has been shown to help with potentially reducing bias or identifying sources of bias in the underlying data by observing the factors of variation. Those who will benefit from this research will be users of generative models, who wish to disentangle or evaluate the disentanglement of particular models for downstream use. This may include artists or photo editors who use generative models for image editing. For negative consequences, this research broadly advances research in deep generative models, which have been shown to have societal consequences when applied maliciously, e.g. mimicking a political figure in DeepFakes.